energies

MDPI

Article

Power Management of the DC Bus Connected Converters in a Hybrid AC/DC Microgrid Tied to the Main Grid

Robert Antonio Salas-Puente *, Silvia Marzal, Raúl González-Medina, Emilio Figueres and Gabriel Garcera

Grupo de Sistemas Electrónicos Industriales del Departamento de Ingeniería Electrónica, Universitat Politècnica de València, Camino de Vera s/n, 46022 Valencia, Spain; silmarro@upv.es (S.M.); raugonme@upv.es (R.G.-M.); efiguere@eln.upv.es (E.F.); ggarcera@eln.upv.es (G.G.)

* Correspondence: rosapue1@posgrado.upv.es; Tel.: +34-(96)-387-7007 (ext. 76021)

Received: 14 February 2018; Accepted: 26 March 2018; Published: 29 March 2018

Abstract: In this paper, a centralized control strategy for the efficient power management of power converters composing a hybrid AC/DC microgrid is explained. The study is focused on the converters connected to the DC bus. The proposed power management algorithm is implemented in a microgrid central processor which is based on assigning several operation functions to each of the generators, loads and energy storage systems in the microgrid. The power flows between the DC and AC buses are studied in several operational scenarios to verify the proposed control. Experimental and simulation results demonstrate that the algorithm allows control of the power dispatch inside the microgrid properly by performing the following tasks: communication among power converters, the grid operator and loads; connection and disconnection of loads; control of the power exchange between the distributed generators and the energy storage system and, finally, supervision of the power dispatch limit set by the grid operator.

Keywords: power management algorithm; microgrid; communication with power converters

1. Introduction

Most countries are dependent on fossil fuels and nuclear energy for electric power generation. However, due to the increasing energy demand and the proliferation of new forms of energy generation which are cheaper and environmentally-friendly, many distributed generation (DG) systems have been integrated into the power grid. Some DGs consist of Renewable Energy Sources (RES), such as Photovoltaic (PV), wind, biomass and geothermal [1]. The DGs are the basis of Microgrids (MGs), which can operate as a single power system that provides a safe and reliable operation at certain voltage and load levels. MGs may work in island-mode or in grid-connected mode, so that they can connect to DGs placed at various locations and inject their energy to the grid if it is needed [2]. The transition between these two operation modes is a process that can destabilize the voltage at the MG buses and damage the MG. In [3], a methodology to recover the MG operation during this transition was presented, along with the main technical problems which should be taken into account. There are three basic MG topologies that can be classified according to the nature of their voltage: DC microgrid (DC MG), AC microgrid (AC MG) and hybrid AC/DC microgrid [4], which is a microgrid with AC and DC buses. Hybrid AC/DC microgrids are currently of great interest to researchers and are considered the distribution and transmission systems of the future, because they enable the coexistence of both AC MGs and DC MGs. The main drawback of the hybrid AC/DC microgrid is the protection strategy because it is more complex than the traditional MG [5,6]. The

large amount of required power converters may complicate the control, management, communication and power dispatch among devices.

Early proposals for the control of a hybrid AC/DC microgrid were presented in [7–9]. In [10] a decentralized control of a MG was proposed, based on using an interlinking converter (ILC) in order to coordinate the power flows among the power converters connected to the AC and DC buses. Droop methods [11] were used to share power among converters. In [10], droop was applied to the power converters connected both to the DC and AC buses. This control concept was extended in [12–14] to implement power interchange among sub-grids comprising a hybrid AC/DC microgrid. Several studies about power management in hybrid AC/DC microgrids using droop strategies for power dispatch have been recently presented [15]. In [16], the droop concept was extended in combination with a cost function defined for the power sharing. Overall, the droop control has a drawback for MGs that result from their small scale. The voltage and the frequency of these systems can fluctuate significantly under load variations or system failures. In order to solve this problem, a communication system between the power converters through a smart centralized system could be used [17–19]. Centralized systems allow optimization of power sharing and integrating different types of RES into the MG. The experimental results of an MG which integrates commercial generators to the distribution grid without any droop control was presented in [20]. In that work, power management of the MG was implemented through an energy management system (EMS). In [21] an EMS was proposed whose aim was to minimize the operational costs of an MG working in grid connected mode. However, local autonomous controllers are necessary in the case of communication failures with the central controller. Those local controllers have been explained in many previous works, such as [22,23]. In [23], a distributed control scheme for the MG was proposed, in which the local controllers were linked to a central controller through a low bandwidth communication device. The central controller managed an optimal EMS.

In this paper a centralized power management algorithm of the DC bus connected DC/DC converters in a hybrid AC/DC microgrid is presented. As shown in Figure 1, the AC bus of the MG is connected to the grid, and the DC bus is connected to the AC bus through an ILC. The ILC is an AC/DC bidirectional converter which regulates the DC bus voltage, managing the power flow between the DC bus and the AC bus. If the microgrid is in island-mode, the distributed generators connected to the AC bus can regulate the AC bus voltage using droop methods. In that case, the ILC can keep regulating the DC bus voltage. The use of centralized communications among all the microgrid elements makes that task feasible [19]. A centralized control decides the status of the DGs, the loads and the energy storage system (ESS) in the MG by applying a set of predefined operation functions. The power exchange with the grid is calculated by an algorithm implemented in the microgrid central processor (MGCP). The algorithm uses the information of the PV available power, the load connected to the DC bus, the battery state of charge (*SOC*) and the power exchange limits provided by the grid operator. The goal of this algorithm is to import the needed power from the grid, keeping it below the limits established by the grid operator, feeding the loads and keeping the *SOC* inside a safe range. If a surplus of energy is available from the PV generation, power is injected to the grid below another limit imposed by the grid operator. It is worth pointing out that this work is focused on the centralized control of the power flow in the MG. It is assumed that each power converter in the MG has a local controller for operating in case of communications failure. The proposed system has a load shedding functionality at the DC bus. This function is performed when the power imported by the microgrid from the grid tends to surpass its pre-defined limits. If there is not enough energy in the distributed generators and batteries, the load shedding functionality will be activated. In addition, in order to avoid the erratic connection/disconnection of loads, a hysteresis level is introduced through a set of power thresholds. The load shedding is used in industrial practice for preventing blackouts, cascading events and the collapse of the power system [24–26].

The main contributions of this manuscript are (i) the definition of twelve operation functions for the management of the DC bus connected converters of the hybrid AC/DC microgrid and (ii) the implementation of load-shedding hysteresis levels in cases where the aim is to keep the battery energy backup as high as possible without exceeding a certain power limit imported from the main

grid. This strategy is usually the preferred one when the electricity tariff is low [27,28]. Moreover, the experimental validation of the centralized power management algorithm in a hybrid AC/DC microgrid is shown. The power management algorithm has been implemented in a MGCP based on TMS320F28335 DSC. Both, the control and the communications of each power converter have been implemented by means of TMS320F28335 DSCs.

This paper consists of five sections. In Section 2, a description of the hybrid AC/DC microgrid under study is provided. In Section 3, several concepts of the power management algorithm are explained. In Section 4, simulation and experimental results at different scenarios of the MG are presented. Section 5 contains the conclusions of the study.

2. Description of the Hybrid AC/DC Microgrid under Study

The hybrid AC/DC microgrid is depicted in Figure 1. The parameters of the communication system inside the MG are shown in Table 1. The MG under study is based on a single DC bus and a single AC bus, connected to the Point of Common Coupling (PCC) of the public grid by means of a static switch. The connection between the DC and AC buses is performed by the ILC, allowing a bidirectional power flow. In grid connected mode, the ILC may work as a current source that injects power to the grid synchronously with the AC bus voltage. An anti-islanding protection, based on [29], has been performed on the DSP of the MGCP. In that case, the operation of the distributed generators connected to the AC bus changes to droop mode so that they can regulate the voltage at the AC bus. The ILC keeps controlling the voltage at the DC bus.

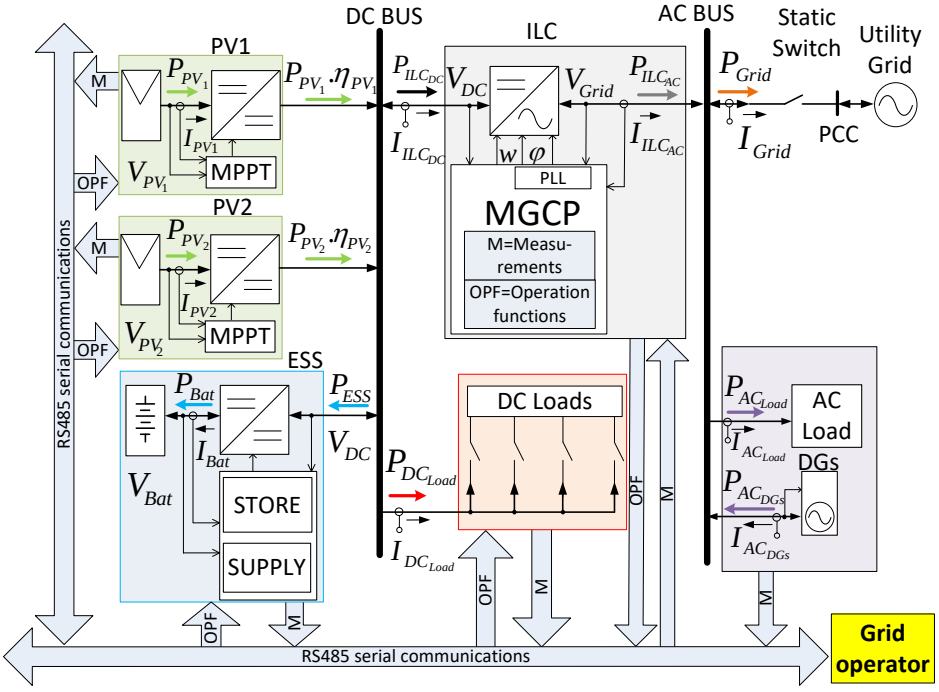

Figure 1. Conceptual scheme of the hybrid AC/DC microgrid under study.

Table 1. Communication parameters of the system.

Communication Parameters between the Devices of the Microgrid (MG) and the Microgrid Central Processor (MGCP)						
	DC MG				**AC MG**	
	ESS	ILC	PV	DC Load	DGs	AC Load
Operations functions	V_{DC_ref} I_{Dis_ref} I_{Ch_ref} VC	φ ω V_{DC_ref}	P_{PV_Lim}	Sw_1 Sw_2 Sw_3 Sw_4		
Measurements	I_{Bat}	I_{ILC_AC}	I_{PV1}	I_{DC_Load}	I_{AC_DGs}	I_{AC_Load}

	V_{DC}	V_{DC}	V_{PV1}	V_{Grid}	V_{Grid}
	V_{Bat}	V_{Grid}	I_{PV2}		
	SOC		V_{PV2}		
Communication Parameters between the MGCP and the Grid Operator					
High-level control			EDL, $\widehat{P}_{Grid\text{-}to\text{-}MG}$, $\widehat{P}_{MG\text{-}to\text{-}Grid}$		

The MGCP sets the operation functions of the power converters, loads and the ESS, depending on the MG scenarios. These scenarios depend on the internal and external changes that affect the power dispatch, such as changes in the solar irradiation, the load, the ESS and the power limit established by the public grid operator.

The MGCP optimizes power sharing by applying several control actions to the microgrid devices: (i) to connect/disconnect the loads as a function of the generated power and the available energy in the batteries; (ii) to share the available power between the priority loads [30] and the ESS; (iii) to adjust the hysteresis levels for avoiding oscillation in the DC bus due the connection-disconnection of loads and (iv) to accomplish the power limits established by the grid operator. Note that the grid operator can establish different power exchange limits at any moment by means of serial communication. In fact, the power generated by the energy sources connected to the DC bus must be limited by the MGCP, in order to prevent an excessive power injection to the public grid beyond the limit set by the grid operator.

The MGCP defines the internal functionality depending on the possible scenarios of the MG. The communications allow control of the PV DGs, the ESS and the load connection/disconnection. In Figure 1, a 10 kW ILC, which connects the AC bus and the DC bus, can be observed. The AC bus is single phase and works in grid-connected mode with a grid voltage: V_{Grid} = 230 V_{rms} and F_{Grid} = 50 Hz ± 1 Hz. In the MG under study, two additional elements are connected to the AC bus: a 5 kW AC DG, and a 4 kW AC load. The nominal DC bus voltage is V_{DC} = 420 V, being regulated by the ILC. Three elements are connected to the DC bus: a 3 kW bidirectional DC/DC converter connected to a battery bank and two 5 kW DC/DC converters connected each one to one PV array. The voltage at the battery bank (V_{Bat}) ranges from 192 V to 252 V, whereas the voltages at the PV arrays (V_{PV1} and V_{PV2}) vary from 306 V to 378 V. Additionally four 'shed-able' 2 kW DC loads are connected to the DC bus. The loads can be connected or disconnected to/from the DC-bus by means of individual switches controlled by the MGCP (*Sw1* to *Sw4*).

3. Management and Control of the MG

3.1. Parameters of the MGCP

In this section, several concepts and parameters of the MGCP are explained in order to define the features and control functionalities of the proposed algorithm.

3.1.1. High-Level Control Limits

The grid operator establishes a tertiary high-level control strategy which controls the power flow between the MG and the main grid. That power flow imposes a limit of the power injected from the MG to the main grid or vice versa. The limits established from the high-level control are:

Energy Dispatch Limit (*EDL*)

The *EDL* is a digital flag that is inside the MGCP which indicates that there is an energy dispatch limit in the MG, set by the grid operator. The *EDL* allows the MGCP to set a suitable control strategy by taking into account the values of the maximum power extracted/injected from/to the grid to/from the MG. When *EDL* = *Off*, there is no energy dispatch limit, and the MGCP can inject or extract unlimited power to/from the grid. In the opposite case (*EDL* = *On*), the MGCP establishes a set of power management criteria which depends on the load connected to the AC or DC buses, the power available in the MG and the *SOC* of the batteries.

Maximum Power Extracted from the Grid

The power flow scenarios between the grid and the MG are shown in Figure 2. Two general cases are possible: $P_{Grid} < 0$ and $P_{Grid} > 0$, being the power flow from the main grid to the microgrid or vice versa. Parameter $\hat{P}_{Grid\text{-}to\text{-}MG}$ is established by the grid operator and represents the maximum power that can be extracted from the main grid to the MG, $|P_{Grid}| \leq \hat{P}_{Grid\text{-}to\text{-}MG}$.

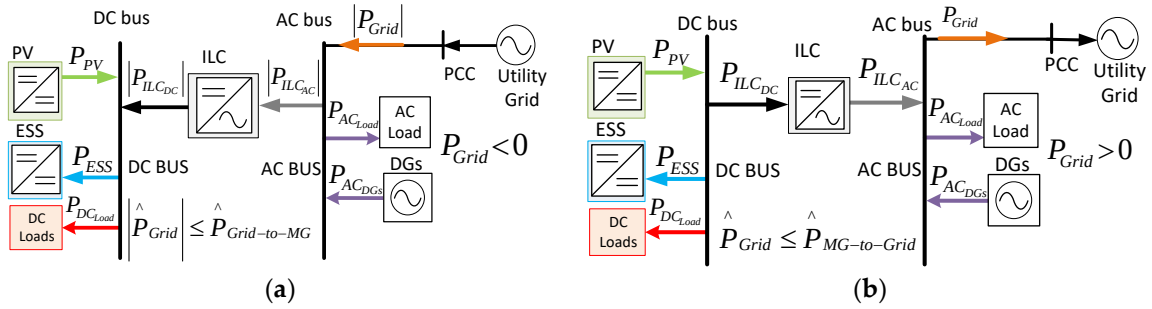

Figure 2. Power flow scenarios between the grid and the MG: (**a**) power flow from the grid to the MG, $P_{Grid} < 0$; (**b**) power flow from the MG to the grid, $P_{Grid} > 0$.

Maximum Power Injected to the Grid

Parameter $\hat{P}_{MG\text{-}to\text{-}Grid}$ stands for the maximum power that can be injected from the MG to the main grid. This parameter is established by the grid operator, imposing the condition, $P_{Grid} \leq \hat{P}_{MG\text{-}to\text{-}Grid}$.

3.1.2. Parameters of the MGCP

The MGCP establishes some parameters for the secondary control strategy, which is responsible for the power flow between the AC bus and the DC bus of the MG. The MGCP must limit the power generated by the RESs, if the available power is higher than that necessary at the MG buses.

Maximum Power Extracted from the AC Bus to the DC Bus Measured at the AC Side of the ILC

The power that flows from the grid to the MG is depicted in Figure 2a. In that case ($P_{Grid} < 0$ and $P_{ILC\_AC} < 0$), the value of P_{ILC_AC} can be calculated by Equation (1). The parameter $\hat{P}_{ILC_{AC}}|_{Grid\text{-}to\text{-}MG}$ stands for the maximum power which can be extracted from the AC bus to the DC bus. This power is measured at the AC side of the ILC (2). The value of $\hat{P}_{ILC_{AC}}|_{Grid\text{-}to\text{-}MG}$ depends on the MGCP, because the value of $\hat{P}_{Grid\text{-}to\text{-}MG}$ is set by the MGCP. The absolute value of P_{ILC_AC} must meet the condition expressed by Equation (3) at any time, taking into account the rated power of the ILC.

$$P_{ILC_{AC}} = P_{AC_{DGs}} + |P_{Grid}| - P_{AC_{Load}} \quad (1)$$

$$\hat{P}_{ILC_{AC}}|_{Grid\text{-}to\text{-}MG} = P_{AC_{DGs}} + \hat{P}_{Grid\text{-}to\text{-}MG} - P_{AC_{Load}} \quad (2)$$

$$|P_{ILC_{AC}}| \leq MIN\left(P_{ILC_{Rated}}, \hat{P}_{ILC_{AC}}|_{Grid-to-MG}\right) \quad (3)$$

Maximum Power Injected from the DC Bus to the AC Bus Measured at the AC Side of the ILC

The power that flows from the MG to the grid is depicted in Figure 2b. In that case ($P_{Grid} > 0$ and $P_{ILC\_AC} > 0$), the value of P_{ILC_AC} can be calculated by Equation (4). Parameter $\hat{P}_{ILC_{AC}}|_{MG\text{-}to\text{-}Grid}$ stands for the maximum power which can be injected from the DC bus to the AC bus, measured at the AC side of the ILC (5). The maximum power injected from the DC bus to the AC bus by the ILC must meet the conditions of Equation (6).

$$P_{ILC_{AC}} = P_{Grid} + P_{AC_{Load}} - P_{AC_{DGs}} \quad (4)$$

$$\hat{P}_{ILC_{AC}}/_{MG\text{-}to\text{-}Grid} = \hat{P}_{MG\text{-}to\text{-}Grid} + P_{AC_{Load}} - P_{AC_{DGs}} \quad (5)$$

$$\widehat{P}_{ILC_{AC}} \leq MIN\left(P_{ILC_{Rated}}, \widehat{P}_{ILC_{AC}}|_{MG-to-Grid}\right) \quad (6)$$

PV Power Generated in the DC Bus

The power outputs generated by the PV DGs connected to the DC bus are measured individually. Parameter P_{PV} is the overall PV power generated in the DC bus of the MG. The total power generated by two PV DC/DC converters connected to the DC bus is shown in Equation (7).

$$P_{PV} = P_{PV1} \cdot \eta_{PV1} + P_{PV2} \cdot \eta_{PV2} \quad (7)$$

Power Consumed by the Loads Connected to the DC and AC Buses

The power consumed by the loads connected to the DC bus is $P_{DC_{Load}} = I_{DC_{Load}} \cdot V_{DC}$ and to the AC bus is $P_{AC_{Load}} = I_{AC_{Load_{rms}}} \cdot V_{Grid_{rms}}$.

Maximum Power Consumed by the Loads Connected to the DC Bus

Parameter $\widehat{P}_{DC_{Load}}$ stands for the maximum overall power which the DC loads are allowed to consume. The load shedding functionality at the DC bus performed by the MGCP depends on this parameter. $\widehat{P}_{DC_{Load}} \leq P_{ILC_{Rated}}$ establishes an upper limit for the maximum power as a function of the ILC power rating.

PV Power Limit

Parameter P_{PV_Lim} is the maximum power that should be extracted from the PV sources at any time, so that it can be consumed by the DC loads and by the batteries ($P_{ESS} > 0$) and/or it injected into the grid. P_{PV_Lim} is represented by Equation (8), where $P_{ESS} = (V_{Bat} \cdot I_{Bat})/\eta_{ESS}$.

$$P_{PV_{Lim}} = \widehat{P}_{ILC_{AC}}/_{MG\text{-}to\text{-}Grid} + P_{DC_{Load}} + P_{ESS} \quad (8)$$

PV Generation Power Available in the DC Bus

Parameter $P_{AvailableDC\_MG}$ is the extra power available from the PV DGs of the DC bus after feeding the load connected in the DC bus. The available PV generation power is defined by Equation (9).

$$P_{Available_{DC\_MG}} = P_{PV} - P_{DC_{Load}} \quad (9)$$

DC Load Switch

The flag of DC load switch takes two possible states, $Sw_{Load} = On$ and $Sw_{Load} = Off$, depending on the connection or disconnection of loads to the DC bus, respectively.

DC Load Hysteresis

Parameter DC_{Load_hyst} is calculated as 10% of the overall power consumed by the DC loads, $DC_{Load_{hyst}} = 0.1 \cdot P_{DC_{Load}}$. DC_{Load_hyst} is the hysteresis level which has been established for avoiding erratic connection/disconnection of the loads.

Power Consumed for the Batteries to C10

Parameter $PESS_{C10}$ is the maximum power consumption for the charge of the batteries of the ESS, $PESS_{C10} = (V_{Bat} \cdot I_{C10})/\eta_{ESS}$. It has been established that the batteries are charged with a current equal to $I_{C10} = C_{10}/10$, where $C10$ the specified battery capacity (measured in A·h) for a discharge time of 10 h.

3.2. Power Management Algorithm

Several calculations and functions are necessary for the suitable power management of the MG control algorithm. These calculations and functions depend on the *SOC* of the battery, the availability of power in the buses, the limits set by the grid operator and the status of Sw_{Load}.

3.2.1. Operation Functions of the MGCP

The power management algorithm embedded in the MGCP executes 12 operation functions according to the various operating scenarios. The operation functions of the MGCP and their interactions with the power converters of the MG are described in the following paragraphs.

Operation Functions in DC Load Connection Mode (Sw_{Load} = *On*)

*Function 1 (**F1**):* All DC loads are fed. When $SOC \leq SOC_{Full}$ (SOC_{Full} = 100%), the DC/DC converter of the ESS charges the batteries from the DC bus with a current (I_{C10}). The PV DGs work at their maximum power point (MPP), so that *MPPT* = *On*. If there is not enough power available from the PV DGs connected to the DC bus, the ILC can extract the rest of the power from the AC bus with the only restriction being $|\hat{P}_{ILC_{AC}}| \leq P_{ILC_{Rated}}$, taking into account that *EDL* = *Off*.

*Function 2 (**F2**):* All DC loads are fed. When $SOC \leq SOC_{Full}$; the DC/DC converter of the ESS charges the batteries from the DC bus with a current equal to I_{C10}. The PV DGs work at their MPP (*MPPT* = *On*). In this case, the PV DGs connected to the DC bus may produce excess power which can be injected into the AC bus by the ILC if necessary, with the only limitation being its rated power: $\hat{P}_{ILC_{AC}} \leq P_{ILC_{Rated}}$.

*Function 3 (**F3**):* All DC loads are fed. When $SOC \leq SOC_{Full}$; the DC/DC converter of the ESS charges the batteries from the DC bus with a current equal to I_{C10}. The PV DGs do not work at their MPP (*MPPT* = *Off*). In this case the PV DGs connected to the DC bus produce a limited amount of power, because the power which can be injected to the AC bus by the ILC is limited by the grid operator. The power injected from the DC to AC bus by the ILC is given by: $P_{ILC_{AC}} \leq \hat{P}_{ILC_{AC}}|_{MG\text{-}to\text{-}Grid}$. Figure 3 depicts the power dispatch inside the MG after applying the operation functions: *F3*, *F8*, *F10* and *F11*.

*Function 4 (**F4**):* All DC loads are disconnected. When $SOC \leq SOC_{MIN}$ (SOC_{MIN} = 20%), the ESS is in standby mode. The flag Sw_{Load} changes from *On* to *Off*, entering the DC load disconnection mode. The PV DGs work at their MPP (*MPPT* = *On*).

*Function 5 (**F5**):* All DC loads are fed. While $SOC \leq SOC_{Full}$, the DC/DC converter of the ESS charges the batteries from the DC bus with a current equal to I_{C10}. The PV DGs work at their maximum power point (*MPPT* = *On*). The ILC injects the excess power at the DC bus to the AC bus. The power injected to the AC bus must comply with the following conditions: $P_{ILC_{AC}} \leq \hat{P}_{ILC_{AC}}|_{MG\text{-}to\text{-}Grid}$.

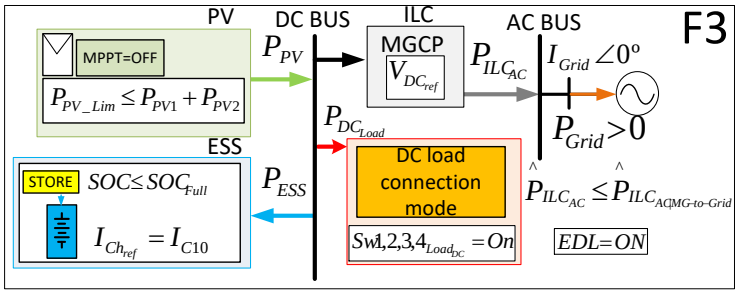

(**a**)

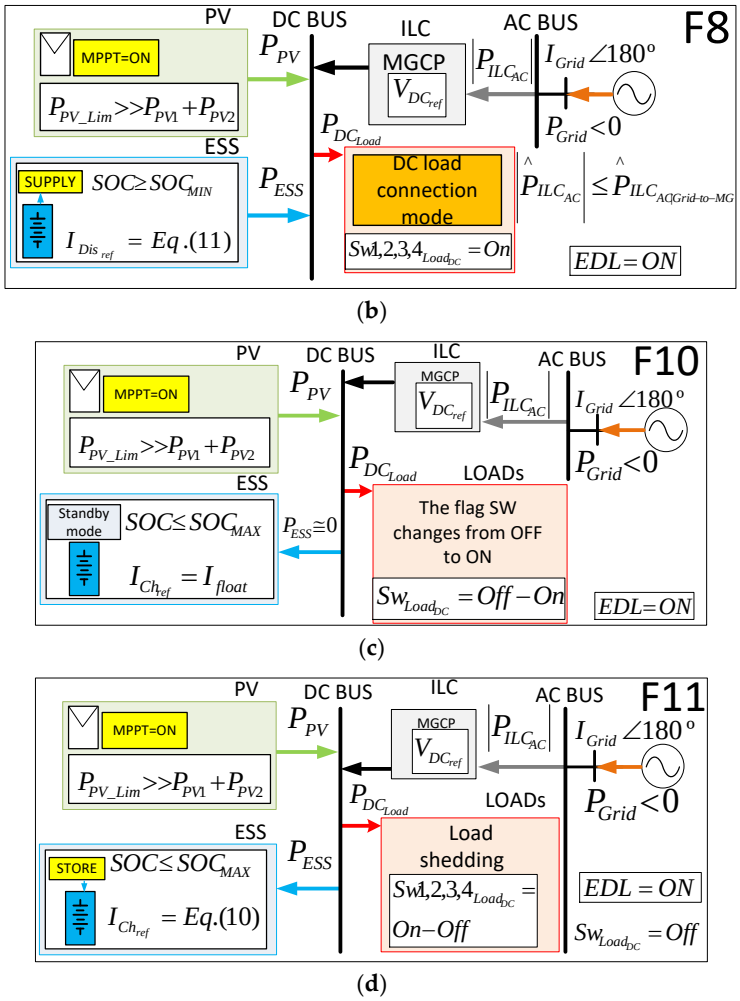

Figure 3. Power dispatch inside the MG after applying the operation functions: (**a**) *F3*; (**b**) *F8*; (**c**) *F10* and (**d**) *F11*.

*Function 6 (**F6**):* All DC loads are fed. As the *SOC* has reached SOC_{FullI}, the DC/DC converter of the ESS stops charging the batteries, putting the ESS in standby mode. The PV DGs work at their MPP (*MPPT* = *On*), producing an excess of power which can be injected to the AC bus by the ILC.

*Function 7 (**F7**):* All DC loads are fed. While $SOC \leq SOC_{FullI}$, the DC/DC converter of the ESS charges the batteries from the DC bus with a current whose value is shown by Equation (10) which is smaller than I_{C10}. The PV DGs work at their MPP (*MPPT* = *On*). If there is not enough power available from the PV DGs, the ILC can extract the rest of power from the AC bus subject to the following limit: $|P_{ILC_{AC}}| \leq \hat{P}_{ILC_{AC}|Grid\text{-}to\text{-}MG}$.

$$I_{Ch_{ref}} = MIN\left(I_{C10}, \frac{P_{Available_{DC\_MG}} + \hat{P}_{ILC_{AC}|Grid-to-MG}}{V_{DC}}\right) \quad (10)$$

*Function 8 (**F8**):* All DC loads are fed. When $SOC \geq SOC_{MIN}$, the DC/DC converter of the ESS operates as a controlled current source discharging the batteries to the DC bus. In *F8*, the PV DGs work at their MPP (*MPPT* = *On*). The sum of the power coming from the ESS and from the PV DGs is not enough to energize the DC loads, so that the required extra power can be transferred from the AC bus to the DC bus through the ILC. That extra power is limited in order not to override the power which can be absorbed by the DC loads. Equation (11) shows the expression of the discharge current. In this case, the extra available power is negative ($P_{AvailableDC\_MG} < 0$), because the power coming from the PV DGs is not enough to energize the DC loads. The power flows in the MG when *F8* is active are shown in Figure 3b.

$$I_{Dis_{ref}} = MIN\left(I_{C10}, \left| \frac{P_{Available_{DC\_MG}} + \hat{P}_{ILC_{AC}}|_{Grid\text{-}to\text{-}MG}}{V_{bat}} \right| \right) \quad (11)$$

*Function 9 (**F9**):* All DC loads are fed. As the *SOC* has reached SOC_{Full}, the DC/DC converter of the ESS stops charging the batteries and enters standby mode. The PV DGs do not work at their maximum power point (*MPPT* = *Off*), because the DC loads cannot absorb the sum of MPP powers. The ILC injects a limited amount of power from the DC to the AC bus which is the required extra power to feed the DC loads.

Operation Functions in DC Load Disconnection Mode (Sw_{Load} = *Off*)

*Function 10 (**F10**):* In *F10*, the flag Sw_{Load} switches from *Off* to *On*. All DC loads are fed. The ESS is in standby mode. The PV DGs work at their MPP (*MPPT* = *On*). The power flows in the MG when *F10* is active are shown in Figure 3c.

*Function 11 (**F11**):* Some DC loads are fed by the load shedding functionality, as is shown in Figure 4. This function each of the DC loads on and off automatically. While $SOC \leq SOC_{MAX}$ (SOC_{MAX} = 80%), the DC/DC converter of the ESS charges the batteries with a current smaller than I_{C10}, given by Equation (10). The power flows in the MG when *F11* is active are shown in Figure 3d. *Cal.0* is the calculation of the available PV power plus the maximum power that can be transferred from the AC bus to the DC bus by the ILC. This expression is shown in Equation (12). A decision tree can be observed in Figure 4, which depicts how 1 to 4 DC loads are connected–disconnected as a function of the value of *Cal.0*. If *Cal.0* is not enough to energize all the DC loads, *F11* begins their disconnection depending on the values of *Cal.0* and the state (1 or 0) of the logic variables, *Comp.1* to *Comp.3*, which are calculated as *AND* functions. Note that a 10% hysteresis band of the power of one DC load has been chosen for establishing the comparison: DC_{Load_hyst} = 0.1·2 kW = 0.2 kW.

$$Cal.0 = P_{PV} + \hat{P}_{ILC_{AC}}|_{Grid\text{-}to\text{-}MG} \quad (12)$$

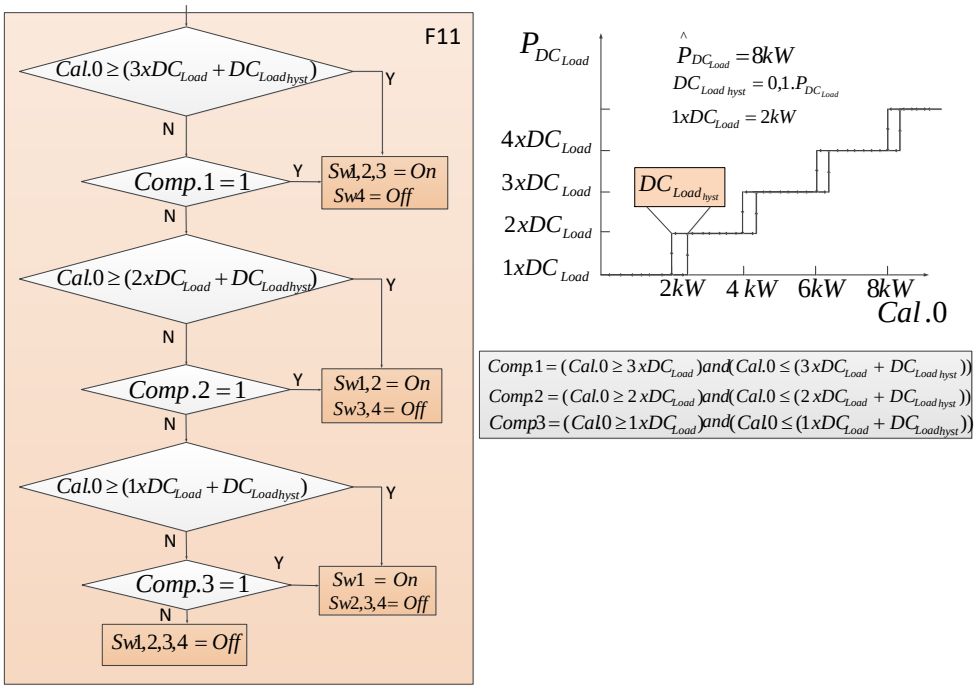

Figure 4. Load shedding functionality.

*Function 12 (**F12**):* All DC loads are fed. When $SOC \leq SOC_{MAX}$, the DC/DC converter of the ESS charges the batteries with a current smaller than I_{C10}, given by Equation (10). The PV DGs work at their MPP (*MPPT* = *On*). If the power coming from the PV DGs is not enough to energize the DC loads, the required extra power can be transferred from the AC to the DC bus through the ILC.

3.2.2. Power Management Algorithm of the MG

The flow diagram of the power management algorithm is shown in Figure 5. *Comp.4* is a logic variable calculated as an OR function. The flags, Sw_{Load} and *EDL*, are fundamental parameters for the power dispatch in the MG. When *EDL* = *Off*, there is no energy dispatch limit, so that functions *F1* or *F2* can be applied. When *EDL* = *On* and Sw_{Load} = *On*, the MGCP applies functions *F3* to *F9*. The flag Sw_{Load} can be turned *Off* by *F4*; after that, the MGCP can apply functions *F10* to *F12*. The functions are implemented so that the power transfer limits between both buses are not exceeded. The calculations performed by the power management algorithm, *Cal.0* to *Cal.4*, are shown in Equations (12)–(15) and allow the power availability of both buses to be checked, taking into account their power dispatch limits.

Equation (13) stands for the power availability in the DC bus coming from DGs and batteries plus the maximum power which can be extracted from the AC bus to the DC bus.

$$Cal.1 = P_{Available_{DCMG}} + \hat{P}_{ILC_{AC}/Grid\text{-}to\text{-}MG} \quad (13)$$

Equation (14) stands for the maximum power that can be injected from the DC to the AC bus plus the power consumed for charging the batteries at a current (I_{C10}).

$$Cal.2 = \hat{P}_{ILC_{AC}/MG\text{-}to\text{-}Grid} + P_{ESS_{C10}} \quad (14)$$

Equation (15) stands for the power available in the DC bus plus the maximum power which can be extracted from the AC bus to the DC bus.

$$Cal.3 = P_{PV} + \hat{P}_{ILC_{AC}/Grid\text{-}to\text{-}MG} - \hat{P}_{DC_{Load}} \quad (15)$$

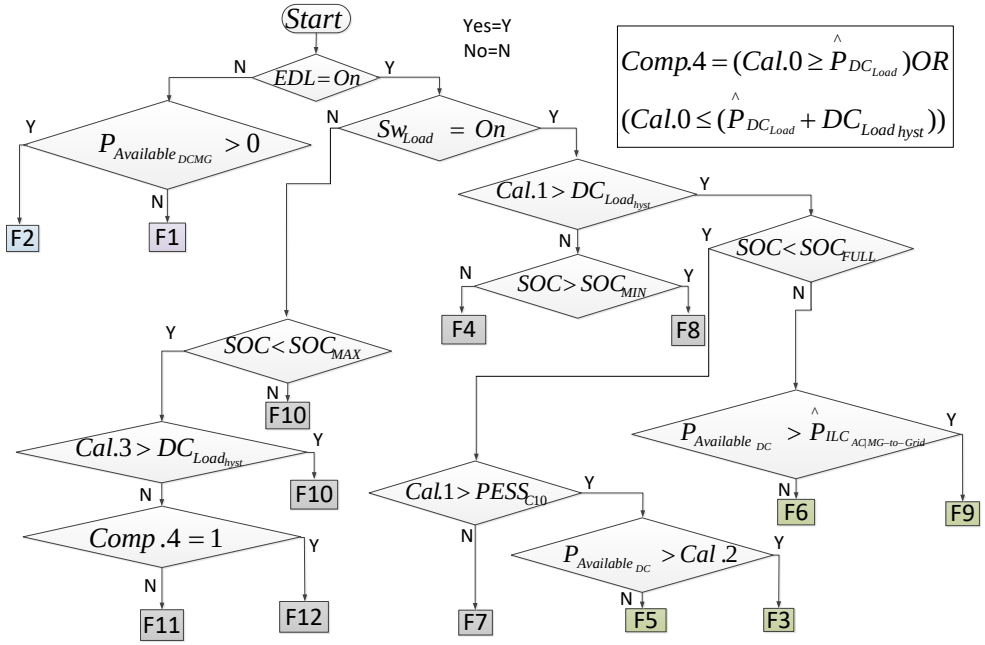

Figure 5. Power management algorithm of the MG.

4. Simulation and Experimental Results

4.1. Simulation Results

The proposed power management algorithm has been simulated by means of PSIM™ [31] under various scenarios. This study is focused on the particular case in which the MG is operating in grid connected mode. The characteristics of the power electronic converters comprising the MG are listed in Table 2. The simulation scenarios of the MG are explained in Table 3. It is worth pointing out that step changes of irradiation shown in Table 3 do not correspond to reality, but they allow us to study the behavior of the MG and the stability of the buses in very extreme cases. In order to check of the

proposed algorithm in different situations with a short simulation time, the algorithm was run in simulations at 25 Hz. The duration of the operation functions *F4* and *F10* is one clock cycle (40 ms), because their main function is to change the load shedding functionality. It is assumed that the ESS is initially discharged ($SOC \leq SOC_{MIN}$). A selected number of possible scenarios have been studied in order to demonstrate the suitable behavior of the MG in its most common and critical situations. In the scenarios under study, step changes of the irradiation, the DC load and the *EDL* were considered, as can be observed in Table 3. The behavior of the proposed algorithm and the application of particular functions *F1* to *F12* by the MGCP can be observed from the following graphs: Figure 6 depicts the behavior of the currents, I_{Bat}, $I_{PV} = I_{PV1} + I_{PV2}$, and of the *SOC* versus time. The evolution of the powers, P_{Bat}, P_{PV}, P_{DCLoad}, P_{ILC_AC} and P_{Grid}, can be observed in Figure 7. Figure 8 provides detail about the most sudden transients of I_{ILC_AC}, V_{DC} and P_{ILC_AC}, which take place throughout the whole simulation, corresponding to the time span, 34.8 s to 35.4 s. The analysis is performed according to the following time intervals:

Interval 1 ($0 \leq t < 1$ s): This interval is divided into two subintervals.

$0 \leq t < 40$ ms: At $t = 0$ s, the ESS is initially discharged ($SOC \leq SOC_{MIN}$). The irradiation is 300 W/m² and the overall DC load absorbs 8 kW. Due to the fact that the PV available power, P_{PV}, at that low irradiation level is not enough to feed the loads, the MGCP applies function *F4*, internally activating flag $Sw_{Load} = Off$.

40 ms $\leq t < 1$ s: After to *F4*, *F11* is applied to disconnect two DC loads (overall *DC load* = 4 kW), and the batteries are charged with a current given by Equation (10).

Table 2. Characteristics of the power converters of the MG.

ILC	2 PV DC/DC Converters (DGs)	ESS
P_{ILC_Rated} = 10 kW V_{Grid} = 230 V F_{Grid} = 50 Hz V_{DC} = 420 V F_{swILC} = 12.8 kHz	$P_{PV1,2\_Boost}$ = 5 kW V_{PV} = 306 V F_{sw_PV} = 16 kHz PV Panel: Atersa A-250P GSE V_{PV_oc} = 37.61 V I_{PV_MAX} = 8.18 A V_{PV_MAX} = 30.58 V I_{PV_CC} = 8.71 A	P_{ESS_HB} = 3 kW V_{Bat} = 216 V F_{sw_ESS} = 16 kHz Battery Bank: 18 batteries type SUN POWER VRM 12V105 connected in series V_{Bat_Nom} = 216 V V_{Bat_MIN} = 185 V V_{Bat_MAX} = 259.2 V $C_{10} \cong$ 105 A·h I_{C10} = 10.5 A

Table 3. The simulation scenarios of the MG.

SIMULATION Scenarios							
Time Intervals (s)							
Time interval number	1	2	3	4	5	6	7
Time span (s)	$0 < t < 1$	$1 < t < 10$	$10 < t < 18$	$18 < t < 20$	$20 < t < 28$	$28 < t < 35$	$35 < t < 40$
Irradiation (W/m²)	300	600	400	800	800	800	100
Load connected to the DC bus	4 loads (8 kW)	4 loads (8 kW)	4 loads (8 kW)	4 loads (8 kW)	2 loads (4 kW)	2 loads (4 kW)	2 loads (4 kW)
$EDL^{(1)}$	*On*	*On*	*On*	*On*	*On*	*Off*	*Off*
ILC	The MG is operating in grid-connection mode						
ESS	The batteries of the ESS are initially discharged. $SOC \leq SOC_{MIN}$						
Power limits	$\hat{P}_{MG-to-Grid}$ = 4 kW, $\hat{P}_{Grid-to-MG}$ = 1kW, $\hat{P}_{DC\,Load}$ = 8 kW						
AC bus	$P_{AC_{Load}}$ = 4 kW, $P_{AC_{DGs}}$ = 5 kW						

[1] Energy dispatch limit.

Interval 2 (1 s $\leq t < 10$ s): At $t = 1$ s, the irradiation undergoes a change from 300 W/m² to 600 W/m², whereas the *SOC* keeps growing below SOC_{MAX}. The MGCP goes on applying *F11*. The PV generation is increased and *F11* connects an additional 2 kW DC load (overall *DC load* = 6 kW) to the DC bus. The MGCP makes both PV DC/DC converters operate at their MPP, whereas the DC bus voltage is regulated to 420 V by the ILC.

Interval 3 (10 s ≤ t ≤ 18 s): This interval is divided into five subintervals.

10 ≤ t < 10.2 s: At t = 10 s, the irradiation decreases from 600 W/m² to 400 W/m², whereas the *SOC* keeps growing below SOC_{MAX}. The MGCP maintains *F11*. The power generated by the panels, P_{PV}, with this irradiation is insufficient to feed three loads, and *F11* disconnects one load (*DC load* = 4 kW) in the DC bus.

10.2 s ≤ t < 10.24 s: At t = 10.2 s the *SOC* surpasses SOC_{MAX}, whereas the irradiation stays at a constant value of 400 W/m². The MGCP applies *F10* after detection of SOC_{MAX}, which internally activates the flag, Sw_{Load} = *On*.

10.24 s ≤ t < 15.4 s: At t = 10.24 s, the generated PV power at the current irradiation level is not enough to feed all the DC loads, so that the MGCP applies *F8* in order to get additional power from the ESS, and the battery bank is discharged at a current given by (11). *F8* connects all DC loads (8 kW) to the DC bus and extracts power from the AC bus taking into account the limit that the maximum power that can be extracted of the same ($|P_{ILC_{AC}}| \leq (\widehat{P}_{ILC_{AC}}|_{Grid\text{-}to\text{-}MG})$, and the ESS injects the current required by the DC bus to feed the DC loads.

15.4 s ≤ t < 15.44 s: At t = 15.4 s the *SOC* goes below SOC_{MIN}, so that the MGCP applies *F4*, internally activating flag Sw_{Load} = *Off*.

15.44 s ≤ t < 18 s: At t = 15.44 s, the MGCP applies *F11*. *F11* disconnects two DC loads (overall *DC load* = 4 kW), so that the batteries are charged with a current given by (10).

Interval 4 (18 s ≤ t < 20 s): At t = 18 s, the irradiation undergoes a linear change of 400 W/m² to 800 W/m², being $SOC < SOC_{MAX}$. The generated PV power and the extracted power from the AC bus are enough to feed all DC loads. Due to limitations on the amount of power that can be interchanged between the buses, the MGCP applies *F12*, and the batteries are charged with a current given by Equation (10). *F12* connects all the DC loads and also sets the PV sources at their MPP.

Interval 5 (20 s ≤ t < 28 s): This interval is divided into three subintervals.

20 ≤ t< 20.04 s: The irradiation keeps a constant 800 W/m² value, whereas *SOC* remains below SOC_{Full}. At t = 20 s, the load connected to the DC bus decreases from 8 kW to 4 kW. The PV-generated power (P_{PV}) at the current irradiation is enough to feed all DC loads. The MGCP applies *F10* which internally activates the flag, Sw_{Load} = *On*.

20.04 ≤ t< 23.7 s: At t = 20.04 s, MGCP applies *F5*. *F5* sets the charge the batteries with a current (I_{C10}). The PV sources work at their MPP. The ILC injects the power excess to the AC bus.

23.7 s ≤ t< 28 s: Both the irradiation (800 W/m²) and the DC load (4 kW) remain constant, whereas the *SOC* has reached 100%. The power generated by the panels is higher than that necessary for feeding the DC loads: P_{PV} > 4 kW. The MGCP applies *F9* to stop charging the batteries and to set the PV generators outside their MPP (*MPPT* = *Off*). In this case, ($P_{ILC_{AC}} \leq \widehat{P}_{ILC_{AC}}|_{MG\text{-}to\text{-}Grid}$).

Interval 6 (28 s ≤ t < 35 s): The irradiation and the *SOC* remain constant: 800 W/m² and 100%, respectively. *EDL* switches from *On* to *Off*. The MGCP applies *F2*, and the ILC injects power into the grid to its rated power, if necessary ($P_{ILC_{AC}} \leq P_{ILC_{Rated}}$). At t = 30 s, MPPT switches from *Off* to *On*.

Interval 7 (35 s ≤ t < 40 s): The irradiation undergoes a change from 800 W/m² to 100 W/m². The MGCP applies *F1*, so that the ILC can extract power from the grid ($|P_{ILC_{AC}}| \leq P_{ILC_{Rated}}$) when *MPPT* = *On*.

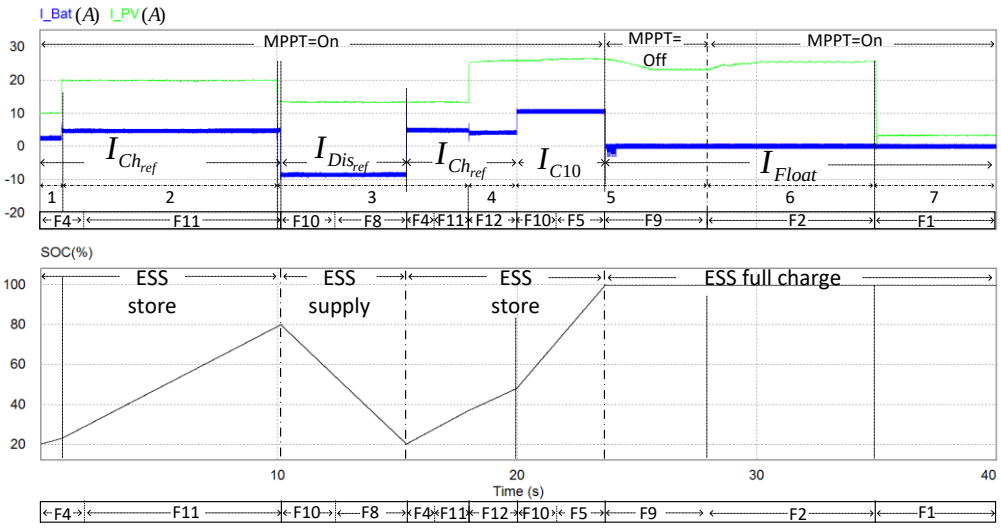

Figure 6. Simulation waveforms, I_{Bat}, $I_{PV} = I_{PV1} + I_{PV2}$ the *SOC* over time.

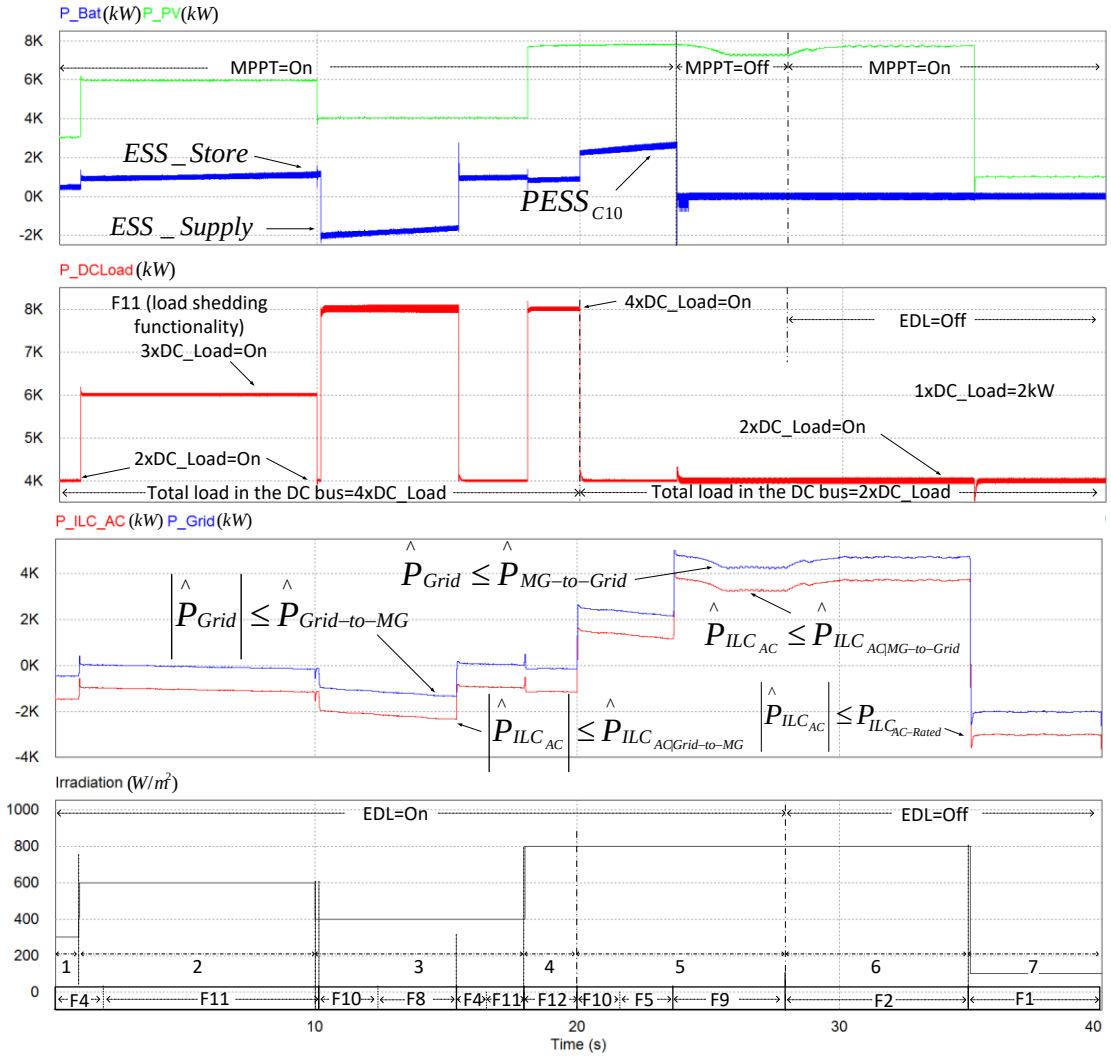

Figure 7. Simulation waveforms of the powers, P_{Bat}, P_{PV}, P_{DCLoad}, P_{ILC_AC} and P_{Grid}.

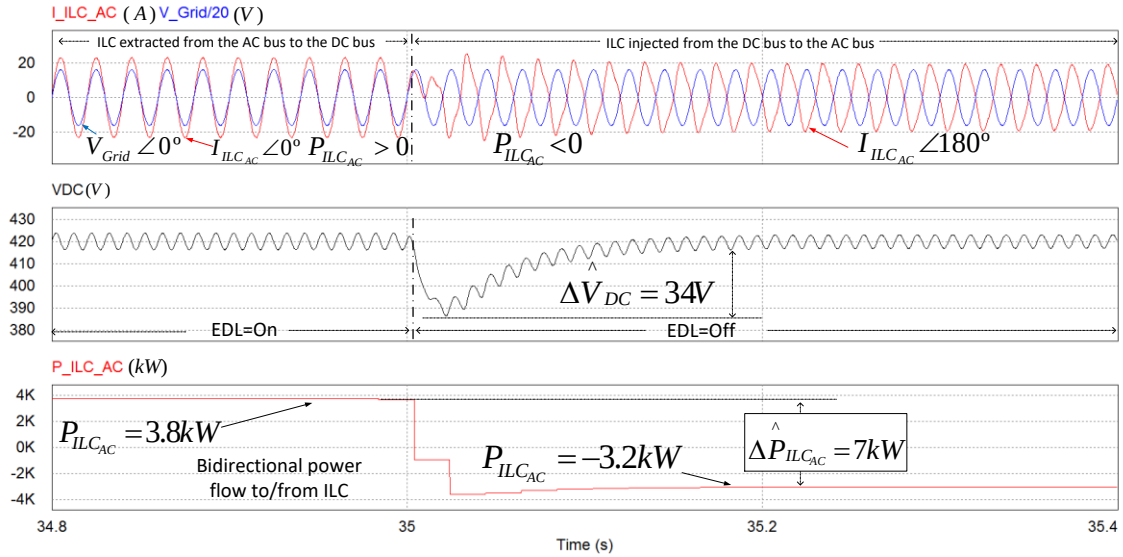

Figure 8. Simulation waveforms of the most sudden transients of I_{ILC_AC}, V_{DC} and P_{ILC_AC}.

4.2. Experimental Results

The experimental power electronic converters, whose characteristics are summarized in Table 2, were built to validate the proposed power management algorithm. The following devices have been connected to the DC bus of the MG available in the lab: a 3 kW battery ESS, a 2.5 kW PV source and four electronic switches to connect/disconnect four DC loads of 0.6 kW ($\hat{P}_{DC_{Load}}$ = 2.4 kW). Figure 9 shows a picture of the experimental setup. The batteries were emulated by a bidirectional DC source/battery emulator, model TC.GSS-Bidirectional-DC-PSU, from Regatron. The PV array was emulated by means of a 10 kW PV array simulator, TerraSAS ETS1000/10, from Ametek (Berwyn, PA, USA). Three experiments were carried out. The experimental scenarios are summarized by Table 4. Figures 10 and 11 depict the waveforms of the currents, voltages and powers of the power converters that form the DC bus of the MG, with Figure 10 corresponding to Experiment 1 and Figure 11 corresponding to Experiment 2. Figure 12 corresponds to Experiment 3.

Experiment 1 and Experiment 2 show the behavior of the system with the same change in the irradiation level at the PV source, but with a different *SOC* of the ESS. The available power injected from the AC bus to the DC bus by the ILC is P_{ILC_DC} = −1 kW.

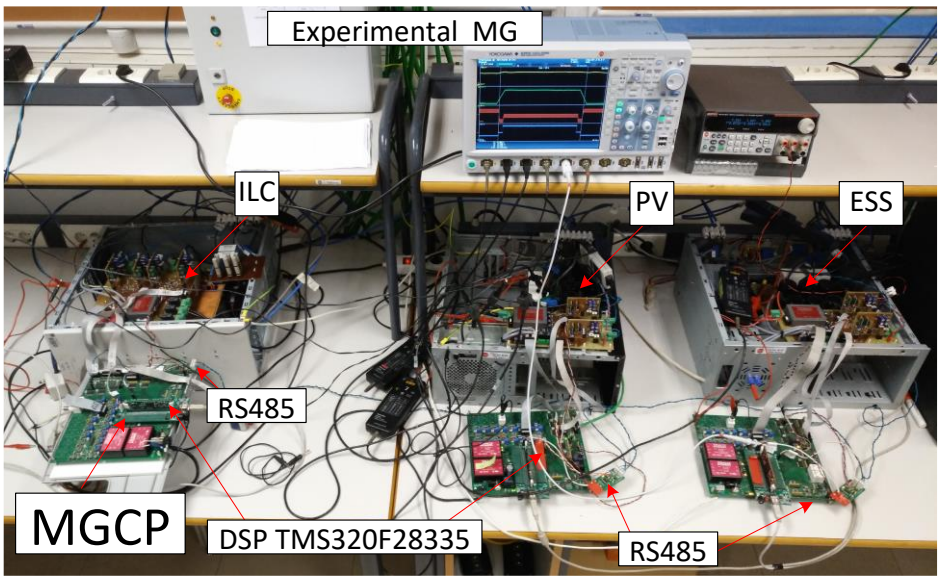

Figure 9. Experimental setup picture.

Experiment 1: The ESS is initially at an $SOC \geq 80\%$ (charged). The four loads remain connected throughout the whole experiment, as can be seen in Figure 10. (P_{DC_Load} = 2.4 kW). The hysteresis level for comparisons with power thresholds is DC_{Load_hyst} = 0.24 kW.

Interval1 1 (0 s < t < 8 s): The irradiation level is 100 W/m² and the PV source works at its maximum power point (MPP), providing P_{PV} = 0.14 kW to the DC bus. That irradiation is not enough to feed all of the loads. Taking into account that the ESS is charged ($SOC \geq 80\%$), the MGCP transfers the maximum possible power from the AC bus (P_{ILC_DC} = −1 kW) to the DC bus through the ILC and applies *F8*. This keeps all the DC loads connected and orders the ESS supplying all the power required by the DC bus, P_{Bat} = −1.26 kW.

Interval 2 (8 s < t < 11 s): The irradiation increases from 100 W/m² to 800 W/m² in 3 s. The MGCP keeps *F8* activated and the power delivered by the ESS can be reduced.

At *t* = 8.6 s, MGCP detects increasing generation, and the PV source works at its MPP, delivering P_{PV} = 0.64 kW. The MGCP keeps *F8* activated and transfers the maximum possible power from the AC bus (P_{ILC_DC} = −1 kW) and keeps all of the DC loads connected. The ESS supplies the power required by the DC bus; the power delivered by the ESS is reduced to P_{Bat} = −0.76 kW.

At *t* = 10.5 s, the PV source works at its MPP delivering P_{PV} = 1.64 kW, with P_{ILC_DC} = −1 kW. At this moment, the MGCP detects that the available power at the DC bus to fed all the DC loads is higher than the hysteresis level ($Cal.1 > DC_{Load\_hyst}$). The MGCP changes from *F8* to *F7*. *F7* forces the ESS to change its operation to energy storage mode; the batteries are charged with a current given by Equation (10). The MGCP changes the setpoint of the ESS charge current, I_{Ch_ref}, until the available power generation is stable (At *t* = 11.6 s, P_{Bat} = 0.5 kW). The power flows in the MG when the MGCP changes from *F8* to *F7* are shown in Zoom 1 of Figure 10.

Table 4. The experimental scenarios of the MG.

Experimental Scenarios [1]					
ESS	Experiment 1: The batteries of the ESS are initially charged. $SOC = SOC_{MAX}$				
Time span (s)	$0 < t < 8$	$8 < t < 11$	$11 < t < 41$	$41 < t < 44$	$44 < t < 50$
Irradiation (W/m²)	100	100–800	800	800–100	100
ESS	Experiment 2: The batteries of the ESS are initially discharged. $SOC \leq SOC_{MIN}$				
Time span (s)	$0 < t < 7$	$7 < t < 10$	$10 < t < 40$	$40 < t < 43$	$43 < t < 50$
Irradiation (W/m²)	100	100–800	800	800–100	100
Load connected to the DC bus	4 loads (2.4 kW)				
EDL	*On*				
ILC	The MG is operating in grid-connection mode				
Power limits	$\hat{P}_{MG-to-Grid}$ = 4 kW, $\hat{P}_{Grid-to-MG}$ = 1 kW, $\hat{P}_{DC_{Load}}$ = 2.4 kW				
AC bus	$P_{AC_{Load}}$ = 4 kW, $P_{AC_{DGs}}$ = 5 kW				

[1] The algorithm is running in the experiments at 1 Hz.

Interval 3 (40.4 s < t < 44.2 s): The irradiation decreases from 800 W/m² to 100 W/m² in 3 s. The MGCP keeps *F8* activated and the power delivered by the ESS can be reduced. The power flows in the MG when *F8* is active are shown in Zoom 2 of Figure 10.

Experiment 2: The ESS is initially at an $SOC \leq 20\%$ (discharged).

Interval 1 (0 s < t < 7 s): The irradiation level is 100 W/m², and the PV source works at its maximum power point (MPP), providing P_{PV} = 0.14 kW to the DC bus. That irradiation is not enough to feed all of the loads. Considering that the ESS is discharged ($SOC < 20\%$), the MGCP transfers the maximum possible power from the AC bus (P_{ILC_DC} = −1 kW) to the DC bus through the ILC and applies the load shedding functionality, *F11*. Taking into account that the available power at the DC bus (1.14 kW) is not enough to feed two loads, *F11* connects only one DC load (0.6 kW). The rest of the available power is used for charging the batteries at P_{Bat} = 0.54 kW. The power flows in the MG when *F11* is active are shown in Zoom 1 of Figure 11.

Interval 2 (7 s < t < 10 s): The irradiation increases from 100 W/m² to 800 W/m² in 3 s. The MGCP keeps function *F11* activated.

At t = 8 s, the PV source works at its MPP, delivering P_{PV} = 0.6 kW, whereas P_{ILC_DC} = −1 kW. At this moment, the MGCP detects that the available power at the DC bus, taking into account the hysteresis level is enough to feed two of the loads. *F11* connects two loads and changes the setpoint I_{Ch_ref} of the ESS from 2.9 A to 0.78 A, where P_{Bat} = 0.15 kW. Note that at t = 8 s, after the connection of the two loads, only $|P_{ILC\_DC}| \leq 0.75$ kW is taken from the AC bus. This ensures a minimum level of power is available in the DC bus.

At t = 9.8 s, the PV source works at its MPP, delivering P_{PV} = 1.7 kW, where P_{ILC_DC} = −1 kW. At this moment, the MGCP detects that the available power at the DC bus to feed all the DC loads is greater than the hysteresis level (DC_{Load_hyst}). The MGCP applies function *F10* which internally activates the flag, Sw_{Load} = *On*. After that, the MGCP starts a transition from *F10* to *F7*. *F7* connects all the DC loads and changes the setpoint of the ESS to I_{Ch_ref} = 1.82 A until the available power generation is stable at the instant t = 11.4 s, where P_{Bat} = 0.35 kW. At t = 9.8 s, the MGCP applies function *F10* during an execution cycle of the algorithm, i.e., for 73 ms. After that, function *F7* is applied.

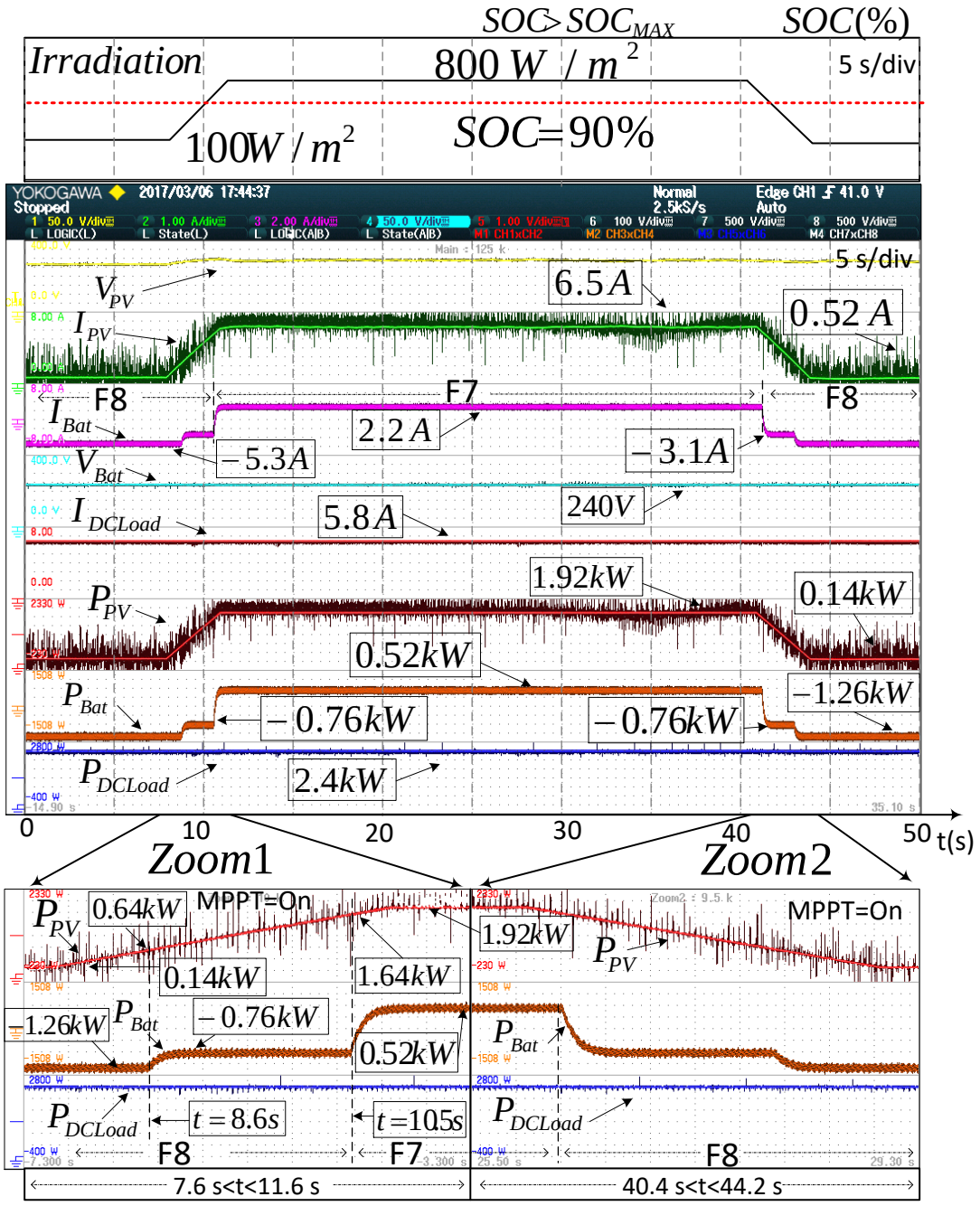

Figure 10. Experiment 1.

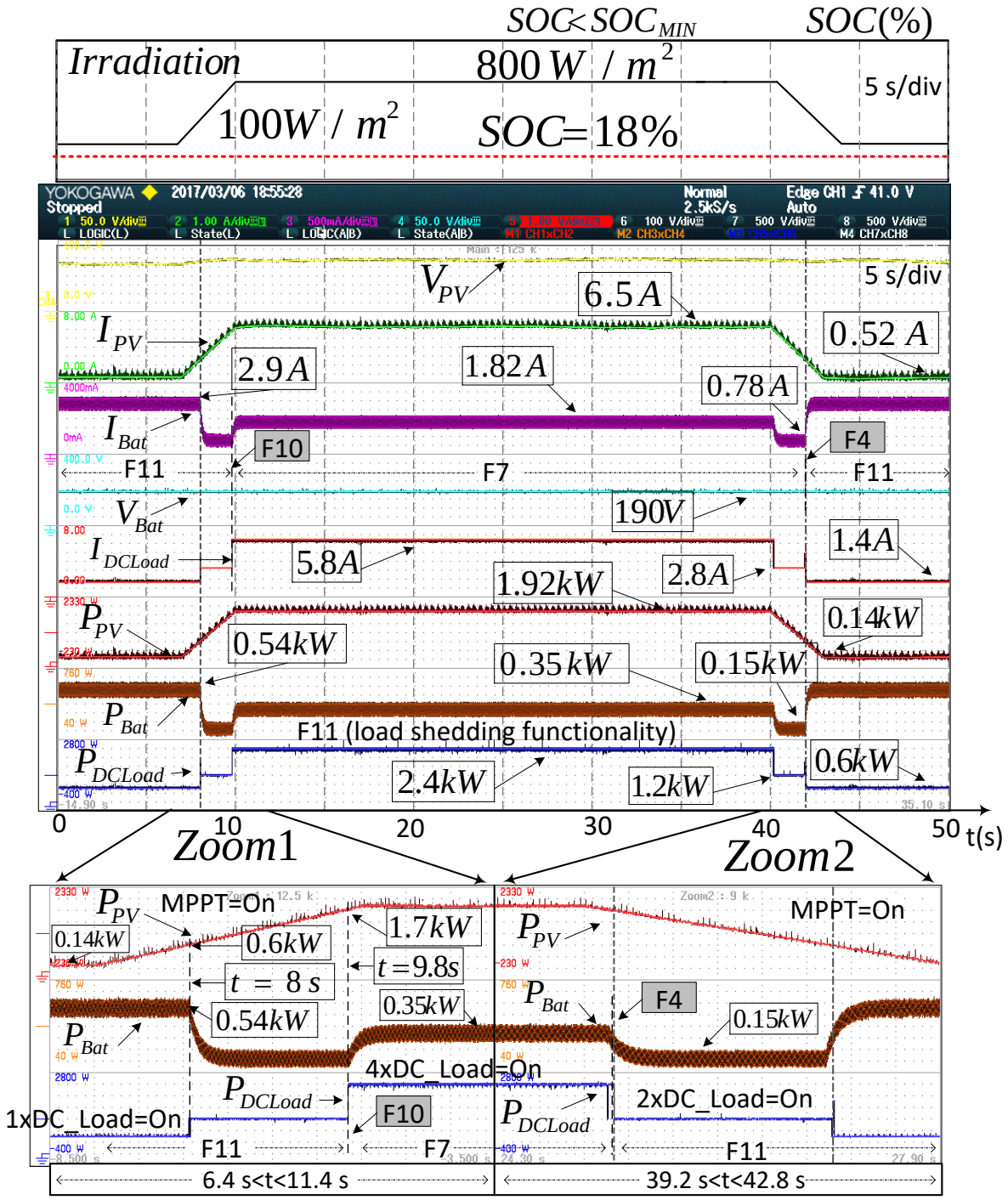

Figure 11. Experiment 2.

Interval 3 (39.2 s < t < 42.8 s): The irradiation decreases from 800 W/m² to 100 W/m² in 3 s. Note that at t = 40 s, the MGCP applies function *F4* which internally activates the flag, Sw_{Load} = *Off*. Then, the MGCP starts a transition from *F4* to *F11*. The MGCP keeps *F11* activated and the power delivered by the ESS can be reduced. The power flows in the MG when the MGCP starts a transition from *F4* to *F11* are shown in Zoom 2 of Figure 11.

Experiment 3: The operation functions broadcasted by the MGCP to the MG elements have a communication delay which depends on the RS485 communication system. In the experimental MG, the computing time of one operation function and its delay to be broadcasted and processed by one of the elements is lower than 74 ms, as can be observed in Figure 12.

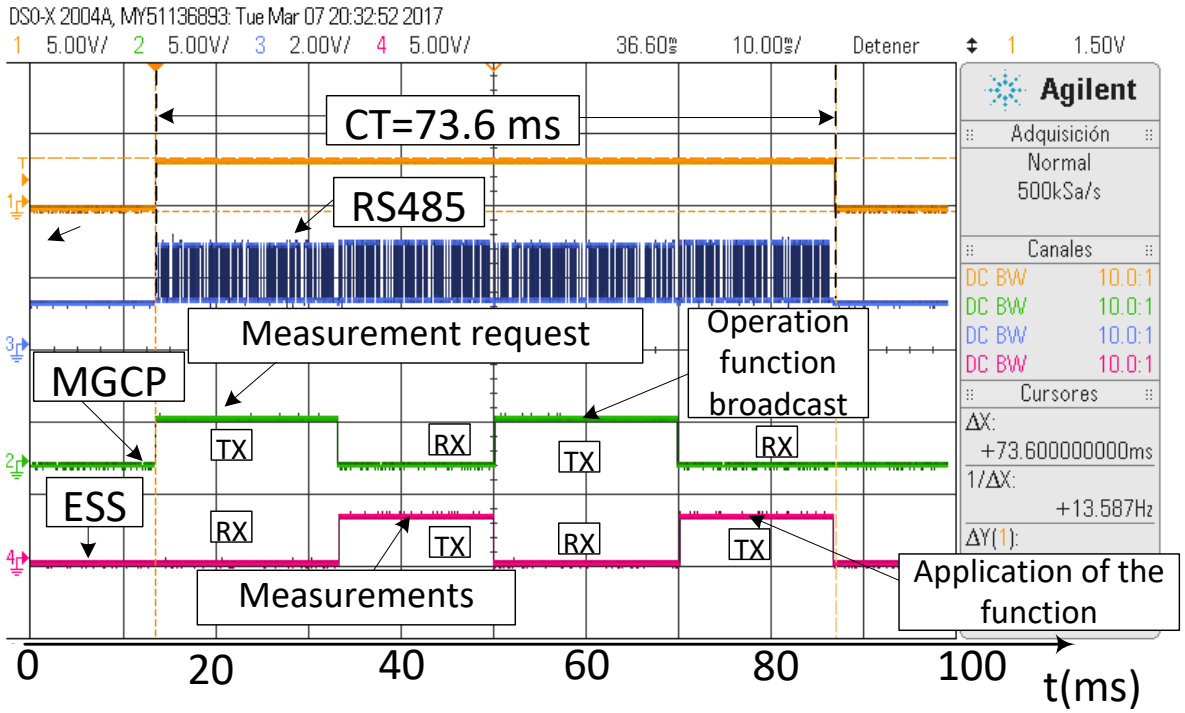

Figure 12. Experiment 3.

4.3. Discussion

In Figure 7, the power exchange between devices of the MG is shown. In the first part of interval 5 ($20 < t < 23.7$ s), the MGCP causes the battery system to be charged to its maximum capacity, $PESS_{C10}$, using the power available from the PV DGs. In the second part of interval 5 ($23.7\text{ s} \leq t < 28$ s), the MGCP limits the generation from the PV DGs, setting their operation points out of the MPP (*MPPT* = *Off*).

The ILC controls the DC bus voltage, because the AC bus works in grid connection mode. The ILC also carries out the synchronization of the AC bus with the grid, causing the current, I_{ILC_AC}, flowing through the ILC to/from the AC bus to have low distortion and to be synchronized with the grid voltage, V_{Grid}, when the MG exports/imports power to the grid. Figure 8 shows the waveforms of I_{ILC_AC} and of V_{Grid} in both situations, where a smooth transient, a good synchronization and a low distortion of I_{ILC_AC} can be observed in the transition from exporting to importing power to/from the AC bus. A smooth transient of the DC bus voltage, V_{DC}, is also observed in that transition at $t = 35$ s, which is the most sudden transient during the whole study, producing a transient undervoltage of $\Delta\hat{v}_{DC} = 34$ V, i.e., less than 10% of the DC bus voltage. It should be considered that the power, P_{ILC_AC}, interchanged between the ILC and the AC bus, undergoes an abrupt change from 3.8 kW to −3.2 kW (7 kW step) at $t = 35$ s, provoked by a fast irradiation decrease.

Figure 10 shows the power exchange among the MG devices in Experiment 1. In time intervals 1 and 3, the MGCP applies the operation function *F8*. In this case, the demand of the DC bus is higher than the sum of the available PV power and the power import limit established by the grid operator. In that case, the MGCP requests the ESS to extract energy from the batteries to temporary feed the DC bus. This functionality reduces the cost of the electric bill.

The power flow in the MG after the application of the load shedding functionality can be observed in the zoom areas of Figure 11. No oscillations during those transients are observed.

In Experiment 3, the overall computing + transmission + processing delay of one operation function is 74 ms, where the ESS is at a distance of 2 m from the MGCP. According to the TIA/EIA-485-A standard, the maximum bandwidth at a 1.2 km distance is 100 kbps, which is much higher than the 9600 bps used in the experimental microgrid. The delay of a CAT5e twisted pair wire is less than 10 μs/km [32]. Therefore, if the distance between the ESS and the MGCP increases to 1 km, taking

into account that the messages between the MGCP and the ESS run through the twisted pair four times (see the green and pink waveforms of Figure 12), the overall delay would increase to about 40 μs, i.e., about 0.05% of the total delays considered in the tests (73.6 ms). Further, the proposed algorithm is executed every second in the microgrid under study, so that the communication delays produced by moderate distances up to a few kilometers are not critical.

5. Conclusions

A new algorithm for the efficient management of the power converters of the hybrid AC/DC microgrid working in grid-connected mode has been presented. The algorithm is based on categorizing the devices according to their type: generation, storage, interlinking converter and load. Twelve operations functions have been defined and programmed in a Microgrid Central Processor for managing the power flow in the MG. The choice of the active operation function depends on the status of the distributed generators, the loads, the energy storage system and the energy dispatch limits between the AC and DC buses established by the grid operator. The MGCP broadcasts the set points of each converter through a RS485 communications system. The experimental and simulation results confirm that the proposed power management algorithm allows a suitable power balance among the MG devices when changes in PV generation, load demand and state of charge of the ESS occur. At any time, the power dispatch limits set by the public grid operator can be accomplished.

Acknowledgments: This work has been cofinanced by the Spanish Ministry of Economy and Competitiveness (MINECO) and by the European Regional Development Fund (ERDF) under Grant ENE2015-64087-C2-2.

Author Contributions: Robert Antonio Salas-Puente, Emilio Figueres and Gabriel Garcerá proposed the main idea, conceived and designed the experiments; Robert Salas-Puente and Raúl González-Medina performed the experiments; Silvia Marzal designed the communication; Silvia Marzal and Raúl González-Medina reviewed the article; Robert Salas-Puente, Emilio Figueres and Gabriel Garcerá wrote this paper.

Conflicts of Interest: The authors declare no conflict of interest.

Nomenclature

P_{PV1}, P_{PV2}	Power supplied by the PV arrays 1 and 2
P_{PV}	Total PV power generated by the DC MG
P_{DCLoad}	Total power consumed by the DC loads
P_{Grid}	Power injected from the hybrid AC/DC microgrid to the main grid
P_{ILC_AC}	Power injected from the DC bus to the AC bus by the ILC, measured at the AC side of the ILC
P_{ILC_DC}	Power injected from the DC bus to the AC bus by the ILC, measured at the DC side of the ILC
P_{ESS}	Power absorbed by ESS from the DC bus
P_{Bat}	Battery bank charge power
P_{ACLoad}	Total power consumed by the AC loads
P_{AC_DGs}	Power supplied by the AC DGs
η_{EES}	Efficiency of the ESS
η_{PV1}, η_{PV2}	Efficiency of the PV DC/DC converters 1 and 2
η_{ILC}	Efficiency of the ILC
I_{Grid}	RMS Current injected from the hybrid AC/DC microgrid to the main grid
V_{Grid}	RMS value of the grid voltage
ω	Grid angular frequency
φ	Grid phase
I_{ACLoad}	Total RMS current consumed by the AC loads
I_{DCLoad}	Total current consumed by the DC loads
V_{DC}	DC bus voltage
I_{ILC_AC}	RMS current injected from the ILC to the AC bus
SOC	State of charge of the battery bank
I_{Bat}	Charge current of the battery bank
V_{Bat}	Voltage of the battery bank

I_{Ch_ref}	Reference of the charge current of the battery bank
I_{Dis_ref}	Reference of the discharge current of the battery bank
I_{PV1}, I_{PV2}	Current supplied by the PV arrays 1 and 2
P_{PV_Lim}	Limit of the PV power generation
I_{DCLoad}	Total current consumed by the DC loads
$S_{W1,2,3,4DC\_Load}$	Switches of the DC loads (loads 1 to 4)
EDL	Energy dispatch limit
$\hat{P}_{Grid-to-MG}$	Maximum power drawn from the grid to the hybrid AC/DC microgrid
$\hat{P}_{MG-to-Grid}$	Maximum power injected to the grid from the hybrid AC/DC microgrid
$\hat{P}_{ILC_{AC}}\|_{Grid-to-MG}$	Maximum power drawn from the AC bus to the DC bus measured at the AC side of the ILC
$\hat{P}_{ILC_{AC}}\|_{MG-to-Grid}$	Maximum power injected from the DC bus to the AC bus, measured at the AC side of the ILC
$P_{ILC_{Rated}}$	Rated power of the ILC
$\hat{P}_{DC\,Load}$	Maximum power consumed by the DC loads
$P_{AvailableDC\_MG}$	Power available at the DC bus of the MG
DC_{Load_hyst}	Power hysteresis level used by the load shedding functionality
$PESS_{C10}$	Power drawn by the ESS from the DC bus at a charge current of the battery bank equal to I_{C10}

References

1. Olivares, D.E.; Mehrizi-Sani, A.; Etemadi, A.H.; Cañizares, C.A.; Iravani, R.; Kazerani, M.; Hajimiragha, A.H.; Gomis-Bellmunt, O.; Saeedifard, M.; Palma-Behnke, R.; et al. Trends in Microgrid Control. *IEEE Trans. Smart Grid* **2014**, *5*, 1905–1919.
2. Dragičević, T.; Lu, X.; Vasquez, J.C.; Guerrero, J.M. DC Microgrids—Part I: A Review of Control Strategies and Stabilization Techniques. *IEEE Trans. Power Electron*. **2016**, *31*, 4876–4891.
3. Cagnano, A.; de Tuglie, E.; Cicognani, L. Prince—Electrical Energy Systems Lab: A pilot project for smart microgrids. *Electr. Power Syst. Res.* **2017**, *148*, 10–17.
4. Unamuno, E.; Barrena, J.A. Hybrid AC/DC microgrids—Part II: Review and classification of control strategies. *Renew. Sustain. Energy Rev*. **2015**, *52*, 1123–1134.
5. Liu, X.; Wang, P.; Loh, P.C. A Hybrid AC/DC Microgrid and Coordination Control. *IEEE Trans. Smart Grid* **2013**, *2*, 278–286.
6. Nejabatkhah, F.; Li, Y.W. Overview of Power Management Strategies of Hybrid AC/DC Microgrid. *IEEE Trans. Power Electron.* **2015**, *30*, 7072–7089.
7. Liu, X.; Wang, P.; Loh, P.C. A hybrid AC/DC micro-grid. In Proceedings of the IPEC Conference Proceedings, Singapore, 27–29 October 2010; pp. 746–751.
8. Wang, P.; Liu, X.; Jin, C.; Loh, P.; Choo, F. A hybrid AC/DC micro-grid architecture, operation and control. In Proceedings of the IEEE Power and Energy Society General Meeting, Detroit, MI, USA, 24–29 July 2011; pp. 1–8.
9. Josep Guerrero, J.V. Hierarchical Control of Droop-Controlled AC and DC Microgrids. A General Approach toward Standardization. *IEEE Trans. Ind. Electron.* **2011**, *58*, 158–172.
10. Poh Chiang Loh, S.M. Autonomous Control of Interlinking Converter with Energy Storage in Hybrid AC-DC Microgrid. *IEEE Trans. Ind. Appl.* **2013**, *49*, 1374–1376.
11. De Brabandere, K.; Bolsens, B.; van den Keybus, J.; Woyte, A.; Driesen, J.; Belmans, R. A Voltage and Frequency Droop Control Method for Parallel Inverters. *IEEE Trans. Power Electron.* **2007**, *22*, 1107–1115.
12. Loh, P.C.; Li, D.; Chai, Y.K.; Blaabjerg, F. Autonomous Operation of Hybrid Microgrid with AC and DC Subgrids. *IEEE Trans. Power Electron.* **2013**, *28*, 2214–2223.
13. Aryani, D.R.; Kim, J.-S.; Song, H. Interlink Converter with Linear Quadratic Regulator Based Current Control for Hybrid AC/DC Microgrid. *Energies* **2017**, *10*, 1799.
14. Luo, F.; Loo, K.H.; Lai, Y.M. A hybrid AC/DC microgrid control scheme with voltage-source inverter-controlled interlinking converters. In Proceedings of the 2016 18th European Conference on Power Electronics and Applications (EPE'16 ECCE Europe), Karlsruhe, Germany, 5–8 September 2016; pp. 1–8.
15. Karimi, Y.; Guerrero, J.M.; Oraee, H. Decentralized method for load sharing and power management in a hybrid single/three-phase islanded microgrid consisting of hybrid source PV/battery units. In Proceedings

of the 2016 IEEE Energy Conversion Congress and Exposition (ECCE), Milwaukee, WI, USA, 18–22 September 2016; pp. 1–8.
16. Hasan, M.A.; Vemula, N.K.; Parida, S.K. Cost based dynamic load dispatch for an autonomous parallel converter hybrid AC-DC microgrid. In Proceedings of the National Power Systems Conference (NPSC), Bhubaneswar, India, 19–21 December 2016; pp. 1–5.
17. Yue, J.; Hu, Z.; Li, C.; Vasquez, J.C.; Guerrero, J.M. Economic Power Schedule and Transactive Energy through an Intelligent Centralized Energy Management System for a DC Residential Distribution System. *Energies* **2017**, *10*, 916.
18. Gao, L.; Liu, Y.; Ren, H.; Guerrero, J.M. A DC Microgrid Coordinated Control Strategy Based on Integrator Current-Sharing. *Energies* **2017**, *10*, 1116.
19. Kaur, A.; Kaushal, J.; Basak, P. A review on microgrid central controller. *Renew. Sustain. Energy Rev.* **2016**, *55*, 338–345.
20. Aluisio, B.; Cagnano, A.; de Tuglie, E.; Dicorato, M.; Forte, G.; Trovato, M. PrInCE lab microgrid: Early experimental results. In Proceedings of the 2016 AEIT International Annual Conference (AEIT), Capri, Italy, 5–7 October 2016; pp. 1–6
21. El-Hendawi, M.; Gabbar, H.A.; El-Saady, G.; Ibrahim, E.-N.A. Control and EMS of a Grid-Connected Microgrid with Economical Analysis. *Energies* **2018**, *11*, 129.
22. Dou, C.; Zhang, Z.; Yue, D.; Zheng, Y. MAS-Based Hierarchical Distributed Coordinate Control Strategy of Virtual Power Source Voltage in Low-Voltage Microgrid. *IEEE Access* **2017**, *5*, 11381–11390.
23. Baek, J.; Choi, W.; Chae, S. Distributed Control Strategy for Autonomous Operation of Hybrid AC/DC Microgrid. *Energies* **2017**, *10*, 373.
24. Tofis, Y.; Timotheou, S.; Kyriakides, E. Minimal Load Shedding Using the Swing Equation. *IEEE Trans. Power Syst.* **2017**, *32*, 2466–2467.
25. Choi, Y.; Lim, Y.; Kim, H.-M. Optimal Load Shedding for Maximizing Satisfaction in an Islanded Microgrid. *Energies* **2017**, *10*, 45.
26. Zhou, H.; Qiu, Y.; Lin, Y.; Wang, Z.; Ma, J. Remote automatic switching and load shedding linkage control scheme. In Proceedings of the 2016 IEEE International Conference on Power and Renewable Energy (ICPRE), Shanghai, China, 21–23 October 2016; pp. 260–263.
27. Grantham, A.; Pudney, P.; Ward, L.A.; Whaley, D.; Boland, J. The viability of electrical energy storage for low-energy households. *Sol. Energy* **2017**, *155*, 1216–1224.
28. Leadbetter, J.; Swan, L. Battery storage system for residential electricity peak demand shaving. *Energy Build.* **2012**, *55*, 685–692.
29. Ciobotaru, M.; Agelidis, V.G.; Teodorescu, R.; Blaabjerg, F. Accurate and less-disturbing active antiislanding method based on PLL for gridconnected converters. *IEEE Trans. Power Electron*. **2010**, *25*, 1576–1584.
30. Faxas-Guzmán, J.; García-Valverde, R.; Serrano-Luján, L.; Urbina, A. Priority load control algorithm for optimal energy management in stand-alone photovoltaic systems. *Renew. Energy* **2014**, *68*, 156–162.
31. *PSIM10.0*; PowerSim: Rockville, MD, USA, 2016.
32. Patrao, I.; González-Medina, R.; Marzal, S.; Garcerá, G.; Figueres, E. Synchronization of Power Inverters in Islanded Microgrids Using an FM-Modulated Signal. *IEEE Trans. Smart Grid* **2017**, *8*, 503–510.